

# Engineering Transport in Manganites by Tuning Local Non-Stoichiometry in Grain Boundaries

Chiabrera, F., Garbayo, . I., López-Conesa, . L., Martín, G., Ruiz-Caridad, A., Walls, M., Ruiz-González, . L., Kordatos, A., Núñez, . M., Morata, . A., Estradé , . S., Chroneos, A., Peiró, F. & Tarancón, . A.

Author post-print (accepted) deposited by Coventry University's Repository

## Original citation & hyperlink:

Chiabrera, F, Garbayo, I, López-Conesa, L, Martín, G, Ruiz-Caridad, A, Walls, M, Ruiz-González, L, Kordatos, A, Núñez , M, Morata, A, Estradé , S, Chroneos, A, Peiró, F & Tarancón, A 2019, 'Engineering Transport in Manganites by Tuning Local Non-Stoichiometry in Grain Boundaries' *Advanced Materials*, vol. 31, no. 4, 1805360. <https://dx.doi.org/10.1002/adma.201805360>

DOI 10.1002/adma.201805360

ISSN 0935-9648

ESSN 1521-4095

Publisher: Wiley

**This is the peer reviewed version of the following article: Chiabrera, F, Garbayo, I, López-Conesa, L, Martín, G, Ruiz-Caridad, A, Walls, M, Ruiz-González, L, Kordatos, A, Núñez , M, Morata, A, Estradé , S, Chroneos, A, Peiró, F & Tarancón, A 2019, 'Engineering Transport in Manganites by Tuning Local Non-Stoichiometry in Grain Boundaries' *Advanced Materials*, vol. 31, no. 4, 1805360. which has been published in final form at 10.1002/adma.201805360. This article may be used for non-commercial purposes in accordance with Wiley Terms and Conditions for Self-Archiving.**

Copyright © and Moral Rights are retained by the author(s) and/ or other copyright owners. A copy can be downloaded for personal non-commercial research or study, without prior permission or charge. This item cannot be reproduced or quoted extensively from without first obtaining permission in writing from the copyright holder(s). The content must not be changed in any way or sold commercially in any format or medium without the formal permission of the copyright holders.

This document is the author's post-print version, incorporating any revisions agreed during the peer-review process. Some differences between the published version and this version may remain and you are advised to consult the published version if you wish to cite from it.

DOI: 10.1002/((please add manuscript number))

**Article type: Communication**

## **Engineering Transport in Manganites by Tuning Local Non-Stoichiometry in Grain Boundaries**

*F. Chiabrera, I. Garbayo, L. López-Conesa, G. Martín, A. Ruiz-Caridad, M. Walls, L. Ruiz-González, A. Kordatos, M. Núñez, A. Morata, S. Estradé, A. Chroneos, F. Peiró, A. Tarancón\**

F. Chiabrera, Dr. I. Garbayo, Dr. M. Núñez, Dr. A. Morata, Prof. Dr. A. Tarancón  
Department of Advanced Materials for Energy, Catalonia Institute for Energy Research (IREC), Jardí de les Dones de Negre 1, Planta 2, 08930 Sant Adrià de Besòs (Barcelona), Spain.

Dr. L. López-Conesa, G. Martín, A. Ruiz-Caridad, Dr. S. Estradé, Prof. Dr. F. Peiró  
Department of Electronics and Biomedical Engineering, University of Barcelona, C. de Martí i Franquès 1, 08028 Barcelona, Spain.

Dr. L. López-Conesa, G. Martín, A. Ruiz-Caridad, Dr. S. Estradé, Prof. Dr. F. Peiró  
Institute of Nanoscience and Nanotechnology, University of Barcelona, 08028 Barcelona, Spain.

Dr. L. López-Conesa  
TEM-MAT Unit, Scientific and Technological Centers of the University of Barcelona (CCiTUB), C. de Lluís Solé i Sabarís 1, 08028 Barcelona, Spain.

M. Walls  
Laboratoire de Physique des Solides Bldg. 510, CNRS, Université Paris-Sud, Université Paris-Saclay, Orsay Cedex, 91405 France.

Prof. Dr. L. Ruiz-González  
Departamento de Química Inorgánica, Facultad de CC. Químicas, Universidad Complutense de Madrid, 28040 Madrid, Spain.

A. Kordatos, Prof. Dr. A. Chroneos  
Faculty of Engineering, Environment and Computing, Coventry University, Priory Street, Coventry CV1 5FB, United Kingdom.

Prof. Dr. A. Chroneos  
Department of Materials, Imperial College London, London SW7 2AZ, United Kingdom.

Prof. Dr. A. Tarancón  
ICREA, Passeig Lluís Companys 23, 08010 Barcelona, Spain.

E-mail: atarancon@irec.cat

Keywords: grain boundary, manganites, nanoionics, interface-dominated materials, local non-stoichiometry

Interface-dominated materials such as nanocrystalline thin films have emerged as an enthralling class of materials able to engineer functional properties of transition metal oxides widely used in energy and information technologies. In particular, it has been proved that strain-induced defects in grain boundaries of manganites deeply impact their functional properties by boosting their oxygen mass transport while abating their electronic and magnetic order. In this work, the origin of these dramatic changes is correlated for the first time with strong modifications of the anionic and cationic composition in the vicinity of strained grain boundary regions. We are also able to alter the grain boundary composition by tuning the overall cationic content in the films, which represents a new and powerful tool, beyond the classical space charge layer effect, for engineering electronic and mass transport properties of metal oxide thin films useful for a collection of relevant solid state devices.

Perovskite manganites with general formula  $RE_{1-x}B_xMnO_{3\pm\delta}$  (where RE stands for a trivalent Rare-Earth element and B for a divalent alkaline ion) have been extensively investigated for their wide variety of intriguing properties, such as oxygen electrocatalysis in solid oxide fuel cell (SOFC),<sup>[1,2]</sup> colossal magnetoresistivity,<sup>[3,4]</sup> resistive switching<sup>[5,6]</sup> and magnetocaloric effect.<sup>[7,8]</sup> Classically, engineering the electro-chemo-mechanical properties in such materials (either bulk or thin films) was reached by the selection of the RE element and/or by doping the A-site with aliovalent atoms. However, in the last years the study of interface-dominated thin films has opened new horizons in the understanding and control of functional transition-metal oxides. For instance, the control of the strain imposed by a substrate in epitaxial thin films was demonstrated to have a large impact on many different aspects, such as the electronic and magnetic properties,<sup>[9,10]</sup> or the oxygen surface exchange rate.<sup>[11]</sup> In addition to the study of pure strain effects, also structural defects, such as dislocations or grain boundaries (GBs), have been shown to strongly influence the overall properties of manganites.<sup>[8,12–16]</sup>

It was recently discovered that GBs in  $La_{0.8}Sr_{0.2}MnO_{3\pm\delta}$  (LSM) thin films are responsible for a substantial enhancement of oxygen diffusion and oxygen reduction reactions (ORR),<sup>[13,14,17]</sup> contrary to what is determined in many oxides where the GBs are known to hinder the oxygen mobility.<sup>[18,19]</sup> The improvement of oxygen mass transport properties is able to completely change the nature of the material converting the mainly electronic LSM into a good mixed ionic-electronic conductor (MIEC). Moreover, it was also determined that dislocations in epitaxial compressive thin films can accelerate oxygen diffusion, suggesting an interesting similarity with the behaviour of the GBs.<sup>[16]</sup> This substantial difference between LSM and other oxides is at the centre of an important debate within the scientific community, since the comprehension of the phenomena might open new horizons to take advantage of GB peculiarities in several families of solid state electrochemical devices.

Alternatively, GBs are also known to deeply impact the electronic and magnetic properties of manganites, generally giving rise to a highly insulating and magnetically disordered region,<sup>[12,20,21]</sup> which can strongly affect, among others, the performance of magnetic cooling devices<sup>[8]</sup> or magnetic memories.<sup>[22]</sup> Since the electronic transport properties of manganites are determined by the chemical and structural order of Mn,<sup>[3,23]</sup> phenomena occurring at the GB level such as lattice strain, cation deficiency and variable oxygen concentration will certainly have an impact on the electronic behaviour.

In this direction, the present study correlates structural and local compositional changes in the vicinity of GBs with the changes observed in the electrochemical and electronic behaviour of LSM thin films, revealing the origin of both their superior ORR catalysis and their deleterious higher resistivity. Ultimately, we prove that the modification of the local composition at the GB level allows tuning these electrochemical, electronic and magnetic properties thus proposing a new and effective tool for engineering the functionality of these, and other technologically relevant materials.

To understand the correlation between the superior performance of dense LSM layers and their local structure, we first prepared Mn-deficient polycrystalline films by means of Pulsed Laser Deposition (PLD) on top of yttria stabilized zirconia (YSZ)-based substrates (YSZ/Si<sub>3</sub>N<sub>4</sub>/SiO<sub>2</sub>/Si), using a proper selection of deposition parameters.<sup>[24–26]</sup> LSM films showed a fully dense polycrystalline structure, with well-defined nanometric columnar grains of tens of nanometers in diameter (**Figure 1a** and **1b**) and a Mn/(La+Sr) ratio of  $B/A = 0.85 \pm 0.02$ , as measured by Wavelength Dispersive Spectroscopy (WDS). High Resolution Transmission Electron Microscopy (HR-TEM) images of the cross section (**Figure 1c**) revealed the good crystallinity of the LSM grains and the absence of secondary phases neither at the GB nor at the core of the columnar-like grains. The most relevant feature of the grain boundaries, observed after Fourier filtering of HRTEM images, is the presence of a high concentration of ordered lattice defects with a periodicity of  $\sim 1$ nm (**Figure 1d**, see also

**section S.1.** of the supplementary information). Higher magnification images show the existence of a regular dense array of dislocations, consisting of a missing atomic plane one out every five (**Figure 1e**). This dislocation network imposes an elastic stress field that propagates for several nanometers inside the grains. Eventually, due to the short distance between the dislocations, the strain field overlaps determining a strained region far beyond the grain boundary core.<sup>[27]</sup>

The effect of these highly defective GBs on the chemical composition was analysed by high angle annular dark-field (HAADF) and electron energy-loss spectroscopy (EELS). First, HAADF (**Figure 2a**) clearly showed a strong contrast associated to the defective region, indicating a local variation in the atomic number likely related to deviations from the bulk grain stoichiometry. More precisely, EELS analysis across and along the grain boundary (**Figure 2b and 2d**, respectively) revealed this significant variation in the atomic composition. Across the interface, **Figure 2b**, we observed an increase of the concentration of Sr and La coupled to a decrease in Mn and O, common to all GBs analysed (see also **Figure S4** in the Supplementary Information). Importantly, despite the stoichiometry deviation, a constant Mn L<sub>23</sub> ratio of *ca.* 2.5 (corresponding to a Mn oxidation state of  $\sim 3.4$ )<sup>[28]</sup> was measured across the GB (**Figure S5**). Moreover, the EELS measurements along the GB interface, **Figure 2c**, yielded analogous compositional variations with complementary La and Mn profiles when crossing the local strain fields created by the dislocations (**Figure 2d**). This latter observation suggests that the strained regions generated by the dislocations are strongly related with the local variation of the stoichiometry. Although the observed oxygen deficiency is fully compatible with the well-known reducing nature of dislocations,<sup>[18,29–31]</sup> the presence of a cation rearrangement (combined with the constant oxidation state of Mn) indicates a more complex charge compensation mechanism than the classical space charge layer formation. The presence of large concentration of manganese vacancies in the bulk ( $B/A = 0.85 \pm 0.02$ ) suggests an interdependence between the grain interior and the GBs, opening the way for

tuning the local non-stoichiometry at the GB level by controlling the overall cationic content in the films.

We therefore investigated the possibility of tuning the ionic composition in the GBs and thus, the functional properties of the LSM films. For this purpose, combinatorial pulsed laser deposition (c-PLD) was employed to generate a thin film with a continuous map of compositions  $\text{La}_{0.8}\text{Sr}_{0.2}\text{Mn}_y\text{O}_{3\pm\delta}$  ( $\text{LSM}_y$ ,  $y = 0.85\text{-}1.2$ ). LSM and  $\text{Mn}_3\text{O}_4$  targets were used as parent compounds, as shown in **Figure 3a** (see **section S.3.1.** for further details on the fabrication process). High quality and dense polycrystalline thin films with variable content of Mn were grown on different substrates, as confirmed by Scanning Electron Microscopy (SEM) and Energy Dispersive X-ray (EDX) analysis (**section S.3.2.** includes a complete structural characterization of the combinatorial film). Importantly, the structural characterization of the  $\text{LSM}_y$  film carried out by X-Ray Diffraction (XRD) confirmed the absence of secondary phases in the whole Mn/(La+Sr) range under study and independently of the substrate, indicating that the Mn was effectively introduced in the perovskite structure (**Figure 3b**). The expected continuous increase of the pseudo-cubic lattice parameter  $c_{pc}$  in the Mn-deficient part together with negligible variations in the La-deficient part was obtained (**Figure 3c**).<sup>[32,33]</sup> Analogously to the study of Mn-deficient LSM films, HAADF and EELS analysis of the  $\text{LSM}_y$  layers was carried out by TEM. Here, a clear impact of the change in the bulk stoichiometry on the local cation composition at the grain boundary level was observed, see representative GBs for each composition in **Figure 3d-k**. The analysis reflects that the GBs suddenly pass from a Mn-deficient state to a La-deficient with the overall Mn content, presumably changing the defect chemistry and giving rise to two different types of GBs, with opposite cation depletion (for a discussion on the quantitative variations we refer to section S.3.3 in the Supplementary Information). Notably, oxygen deficiency was found in all the GBs, independently on the Mn content (see **Figure S14** in the Supplementary Information). In order to assess the impact of the local non-stoichiometry of the GBs on the transport

properties of the  $\text{LSM}_y$  films, we evaluated for the whole series of compositions both the in-plane electrical conductivity (measured on insulating substrates, Sapphire (0001) and  $\text{YSZ}/\text{Si}_3\text{N}_4/\text{SiO}_2/\text{Si}$ ) and the electrochemical properties (on an oxygen ion conducting electrolyte,  $\text{YSZ}$  (001)), see **Figures 4a and 4b** respectively. First, we focus on the changes observed in the electrical properties, **Figure 4c**. Here, we show the evolution of the electronic resistivity as a function of temperature ( $T= 85\text{-}575$  K) for the polycrystalline  $\text{LSM}_y$  series on a sapphire substrate. Note that, for comparison, the plot also includes results obtained for a 60 nm-thick epitaxial LSM film, grown on an  $\text{NdGaO}_3$  (110) substrate under the same deposition conditions than the polycrystalline  $\text{LSM}_{0.85}$  (see **section S.2.** for a complete characterization). This epitaxial film is expected to behave mostly like the grain interior of polycrystalline  $\text{LSM}_{0.85}$  and is taken as a reference to ensure that the effects observed are associated to the GBs. Indeed, the polycrystalline and epitaxial  $\text{LSM}_{0.85}$  thin films present the same bulk cationic composition, Mn oxidation state and, consequently, oxygen content.<sup>[34]</sup> As shown in **Figure 4c**, the epitaxial  $\text{LSM}_{0.85}$  film (blue open symbols) indeed presents a metal-insulator (M-I) transition typical of bulk stoichiometric manganites. Although a suppression of M-I transition was previously reported for Mn deficient compositions,<sup>[24,35,36]</sup> the absence of extended structural defects (GBs) in the epitaxial films preserves the long range electronic order, allowing the onset of metal behaviour. Opposed to that, the polycrystalline counterpart ( $\text{LSM}_{0.85}$ ) presents at least one order of magnitude higher resistance together with the suppression of the M-I transition. Moreover, it is important to note that no changes in the electrical resistivity were observed after annealing at temperatures as high as 923 K for 5 hours, suggesting a strong equilibrium of the GB (see **Figure S17** in Supplementary Information). Remarkably, as shown in **Figure 4c**, progressively increasing the B/A ratio leads to a continuous decrease of the resistivity recovering the low temperature M-I transition for  $\text{Mn}/(\text{La}+\text{Sr}) > 0.92$  (complementary results were obtained for the  $\text{YSZ}/\text{Si}$  substrate as shown in the supplementary information, **Figure S18**).

This M-I transition in manganites has been traditionally interpreted as a Jahn-Teller (JT) mediated double-exchange mechanism, consisting of the transfer of one electron between two ferromagnetic spin-aligned Mn ions through the oxygen orbital.<sup>[37,38]</sup> In the Mn-deficient LSM GBs (see **Figure 2**), the simultaneous decrease of O and Mn is expected to strongly impede the metallic behaviour due to the interruption of the Mn-O-Mn chains and the formation of a highly insulating zone of the width of the local non-stoichiometry. The recovery of the M-I transition in the polycrystalline thin films well correlates with the change of GB composition observed increasing the overall B/A ratio (see **Figure 3**). In these Mn-rich GBs, the decrease of La is not supposed to affect the electronic transport, while the progressive increase of Mn helps to restore the metallic long-range order, gradually improving the metallic behaviour. It is worth mentioning that also an enhancement of the bulk conductivity was measured in the epitaxial thin films increasing the Mn content (see **Figure S19** in Supplementary Information).<sup>[34]</sup> Nevertheless, the conductivity of the polycrystalline thin films is orders of magnitude lower than the corresponding epitaxial one, meaning that the GB contribution is always dominating the macroscopic electronic transport.

Complementary to the electrical measurements, we carried out the electrochemical characterization of the LSM<sub>y</sub> series as part of LSM<sub>y</sub>/YSZ/Ag cells, where YSZ is a pure ionic conductor acting as an electrolyte and the silver is playing the role of the backside electrode. The study of this type of MIEC-based cells by Electrochemical Impedance Spectroscopy (EIS) allows the determination of their oxygen mass transport properties,<sup>[1]</sup> i.e. the oxygen diffusion coefficient,  $D^*$ , and the surface exchange coefficient,  $k^*$  (see section **S.3.5** for a detailed explanation). The evolution of the oxygen diffusion and surface exchange coefficients obtained by EIS analysis in air at 923K are presented in **Figure 4d** and **e**, respectively. First, a substantial increase of the diffusivity (above two orders of magnitude) with respect to the reported bulk values is observed in all the samples. This confirms the existence of an oxygen fast diffusion pathway along the GBs, independently of the

Mn/(La+Sr) ratio, consistent with the oxygen deficiency observed in all the GB types (**Figure S14**). On top of that, Mn-deficient layers with  $Mn/(La+Sr) < 0.9$  present an additional increase up to two orders of magnitude, for a total of four, in the diffusivity. On one side, these results may be behind the discrepancies observed by different authors in the past,<sup>[13–15]</sup> while on the other they show for the first time the possibility of tuning the diffusivity by controlling the content of Mn. Regarding the surface exchange (**Figure 4e**), an analogous trend to the oxygen diffusion is observed in the Mn deficient GBs. The strong coupling of the two oxygen parameters, along with the observed oxygen depletion in the GBs, corroborate the hypothesis that the accumulation of oxygen vacancies is at the origin of the large improvement of the Oxygen Reduction Reactions (ORR) reported for manganite thin films by different authors.<sup>[17]</sup> This conclusion is also supported by theoretical works from Choi *et al.*<sup>[39]</sup> and Mastrikov *et al.*,<sup>[40]</sup> where the scarce concentration of oxygen vacancies was found as the limiting factor for oxygen incorporation in bulk LSM. The strong implications of our observation contribute to the general understanding of the ORR mechanism for metal transition based perovskites, which is still under debate.<sup>[41–43]</sup> In this direction, a traditional gap of knowledge regarding the unexpected excellent behaviour of a mainly electronic conductor such as LSM bulk is overcome by considering the superior interface performance proved, when the material is not limited by the availability of oxygen vacancies.

With these results we unambiguously show that the origin of the deleterious effects on the electrical behaviour and the superior oxygen mass transport properties rely on the evolution of the nature of the GB, which is dominated by the cation and anion local non-stoichiometry. A transition in the nature of GBs occurs at  $Mn/(La+Sr) \sim 0.9$  in LSM, likely associated to a change in the local defect chemistry. Above this value, slightly Mn-deficient and Mn-rich films are characterized by a significant oxygen vacancies concentration ( $V_O^{\bullet\bullet}$ ), arising from the presence of highly reducing dislocations,<sup>[31]</sup> compensated by lanthanum vacancies ( $V_{La}^{\prime\prime}$ ) and the formation of naturally occurring antisite defects ( $Mn_{La}^{\times}$ ),<sup>[44]</sup> which is fully compatible with

our HRTEM-EELS observations. More interestingly, for highly Mn-deficient layers ( $\text{Mn}/(\text{La}+\text{Sr}) < 0.9$ ), an increasing oxygen diffusivity is observed due to a further increase of the oxygen vacancies concentration, which seems to be strongly interrelated to the decrease in Mn content and the presence of compensating negative defects such as Mn vacancies ( $V_{\text{Mn}}'''$ ) (**Figure 2**). As previously mentioned, this decrease of Mn at the GB level is complemented by an increase of the La and Sr content. This, together with the absence of secondary phases (such as the La-rich Ruddlesden-Popper phase) in the GBs, suggests the formation of the  $\text{La}_{\text{Mn}}^{\times}$  antisite defect. However, this type of defect is hardly formed in strain-free bulk LSM due to the much bigger ionic radius of  $\text{La}^{3+}$  compared to  $\text{Mn}^{3+}/\text{Mn}^{4+}$ .<sup>[45]</sup> Density Functional Theory (DFT) simulations were carried out in this work (see details in the experimental section) to evaluate the formation of these unusual  $\text{La}_{\text{Mn}}^{\times}$  defects in combination with other defects and constrains typically present at the LSM GBs, i.e. strain, the presence of oxygen vacancies and Sr dopants. The formation energies of different defect clusters under variable strain states ( $\epsilon$ ) were calculated to find the most stable defect configurations in the presence of Mn vacancies (see **Table 1**). Several conclusions arise from this analysis: first, the formation of the oversized  $\text{La}_{\text{Mn}}^{\times}$  defect is more favourable in the vicinity of the smaller Sr cations ( $\text{Sr}'_{\text{La}}$ ); second, the formation energy is even lower in the presence of one oxygen vacancy,  $V_{\text{O}}''$  (additional Sr dopants in the cluster do not reduce this value); third, no significant variation was obtained when applying strain in the presence of Sr doping atoms and/or oxygen vacancies. All in all, this indicates that the driving energy for the antisite defect formation in GBs relies on a complex association of defects ( $V_{\text{Mn}}''', \text{Sr}'_{\text{La}}$  and  $V_{\text{O}}''$ ) rather than a classical space charge mechanism.

It is important to note that local cation non-stoichiometry in manganites was also observed in other type of interfaces, e.g. dislocations in epitaxial  $\text{La}_{0.7}\text{Sr}_{0.3}\text{MnO}_3$  on  $\text{LaAlO}_3$ <sup>[46,47]</sup> or purely strained  $\text{La}_{0.7}\text{Sr}_{0.3}\text{MnO}_3/\text{SrTiO}_3$  hetero-interfaces.<sup>[48–50]</sup> This suggests that the compensation

mechanism observed in this work can be generally extrapolated to other strained and oxygen deficient interfaces. The natural presence of cationic vacancies in manganites, even in the nominally stoichiometric material,<sup>[51]</sup> is most likely the main driver of this unusual elemental rearrangement. The GB engineering shown in this work could be therefore extended to other interfaces and, more interestingly, to other perovskites, opening the way for new strategies to control the transport properties of materials by tuning the local non-stoichiometry.

In summary, we revealed the origin of the superior mass transport properties of interface-dominated LSM thin films by directly observing a strain-related accumulation of oxygen vacancies in the GBs that defines high diffusion pathways. We found a strong correlation between these changes and the local cation non-stoichiometry observed at the GB level, which we were able to actively modify for completely change the nature of the interface. Therefore, we present here a new tool for tailoring the transport properties of technologically relevant interfaces such as grain boundaries (beyond the traditional space charge layer engineering) suitable for direct application in a collection of solid state devices based on mixed ionic-electronic conductors, including thin film based solid oxide fuel cells, resistive switching devices, magnetoresistance or supercapacitors.

## Experimental Section

*Films.*  $\text{La}_{0.8}\text{Sr}_{0.2}\text{Mn}_{1-y}\text{O}_{3\pm\delta}$  (LSM) / Ytria-stabilized Zirconia (YSZ) polycrystalline heterostructures (100nm LSM / 100 nm YSZ) were grown by PLD on Si (100) substrates, electrically and stress passivated by 300nm  $\text{Si}_3\text{N}_4$  / 100 nm  $\text{SiO}_2$  bilayers. The PLD system used is a large-area system from PVD Products (PLD-5000), equipped with a KrF-248 nm excimer laser from Lambda Physics (COMPex PRO 205). Commercial targets with nominal composition  $\text{La}_{0.8}\text{Sr}_{0.2}\text{MnO}_3$  (LSM) and 3 mol-%  $\text{Y}_2\text{O}_3$  stabilized  $\text{ZrO}_2$  (3YSZ) were used for the thin films deposition. The films were deposited with an energy fluency of  $1 \text{ J cm}^{-2}$  per pulse at a frequency of 10 Hz. The substrate was kept at 700°C, in an oxygen partial pressure

of 0.026 mbar during the deposition and the substrate-target distance was set to 95mm.

Epitaxial LSM films were deposited under the same conditions of the polycrystalline films on NdGaO<sub>3</sub> (110) substrates. Combinatorial pulsed Laser deposition (c-PLD) technique was used to grow LSM<sub>y</sub> films with variable Mn/(La+Sr) ratio. Commercial targets of LSM and Mn<sub>3</sub>O<sub>4</sub> were used as parent compounds. The deposition conditions used were the same as for the single polycrystalline and epitaxial LSM. LSM<sub>y</sub> combinatorial samples were grown on YSZ/Si 4" wafers and 5mm x 10mm Sapphire (0001) substrates (for the in-plane electrical measurements) and on 3mm x 3mm YSZ (001) single crystal (for the electrochemical measurements). More details on the combinatorial deposition technique can be found in **section S.3.1.** of the supplementary information. The nominal composition of the films was measured by Wavelength Dispersive Spectroscopy (WDS) (model- Jeol JXA-8230) technique and by Energy Dispersive X-ray Analysis. The films were characterized by SEM in a ZEISS AURIGA equipment and by XRD in a four-angle diffractometer with a Cu K $\alpha$  radiation source (X'Pert MRD-Panalytical) and in a Bruker D8 Advance diffractometer system.

*Electrical characterization.* LSM thin films were analysed in 4-points in-plane electrical measurements in a temperature-controlled Linkam probe station, between 83K and 573K (more details can be found in **section S.3.3.1** of the supplementary information).

*Electrochemical characterization.* Electrochemical impedance spectroscopy (EIS) was performed on the LSM<sub>y</sub> combinatorial dense samples deposited on YSZ single crystals with a Novocontrol Alpha-A analyzer. Porous silver paste was painted as backside electrode due to its excellent oxygen electrochemical properties. Porous gold paste was applied on the top of the LSM<sub>y</sub> films for assuring a homogenous current collection. The frequency range chosen was 10<sup>6</sup>-0.05 Hz and an AC voltage with amplitude 0.05 V was applied. The experiments were performed in a ProboStat test station (NorECs) placed inside a vertical furnace. The temperature was set to 650°C and synthetic air was flown into the system.

TEM. HRTEM images were acquired in a JEOL J2010F microscope operated at 200 kV accelerating voltage. EELS experiments were carried out in a JEOL ARM 200cF microscope operated at 200 kV, a FEI TITAN Low Base operated at 300 kV and a Nion UltraSTEM operated at 100 kV.

*DFT simulations.* The calculations were performed using the plane wave DFT code CASTEP.<sup>[52,53]</sup> The exchange and correlation interactions were modelled with the corrected density functional of Perdew, Burke and Ernzerhof (PBE)<sup>[54]</sup> within the generalized gradient approximation (GGA) and ultrasoft pseudopotentials.<sup>[55]</sup> Spin polarized calculations with the Hubbard U contribution were used to account for the strong Coulombic interaction of the localised electrons of the 3d orbitals of Mn (the U value was set to 4 eV). The plane wave basis set was set to a cut-off of 400 eV, in conjunction with a  $2 \times 3 \times 2$  Monkhorst-Pack (MP)<sup>[56]</sup> k-point grid and an 80-atomic site supercell with lattice parameters of  $a = c = 11.1 \text{ \AA}$ ,  $b = 7.73 \text{ \AA}$  and supercell volume of  $954.9 \text{ \AA}^3$ . LMO / LSM is an orthorombic perovskite within the (Pnma) space group (space group number 62). All supercells were geometry optimized and fully relaxed, reaching the ground state of the system. All calculations were under constant pressure conditions. The final configurations were used for the electronic spectroscopy. We employ the OptaDOS subcode<sup>[57,58]</sup> for the projected density of states visualization. The geometry optimized supercells are treated as spin-polarized with a grid of  $7 \times 7 \times 7$  k-points. The band structure is plotted with an analytical step of 0.001 eV.

### Supporting Information

Supplementary Figures S1–S19, Supplementary References 1–22

### Acknowledgements

The research was supported by the Generalitat de Catalunya-AGAUR (2017 SGR 1421) and the European Regional Development Funds (MAT2016-79455-P/FEDER). This project has received funding from the European research Council (ERC) under the European Union's Horizon 2020 research and innovation programme (ULTRASOFC, Grant Agreement number: 681146). Dr. R. Arenal is acknowledged for his support in the TEM analysis. Dr. J. Santiso is acknowledged for his support in the XRD analysis of the epitaxial thin film.

**Author Contributions**

F.C., I.G., A.T., conceived the original idea behind this study. F.C. grew the films, performed the elementary (WDS, EDX), microstructural (SEM, XRD), electrical and electrochemical analysis and wrote the manuscript. I.G. and A.M. supervised and helped with the experimental work and co-wrote the manuscript. L.L.C., G.M., A.R.C., M.W., L.R.G., M.N., S.E., and F.P. carried out the TEM characterization and analysis. A.K. and A.C. contributed with the DFT simulations. A.T. supervised and co-wrote the manuscript.

Received: ((will be filled in by the editorial staff))

Revised: ((will be filled in by the editorial staff))

Published online: ((will be filled in by the editorial staff))

**References**

- [1] S. B. Adler, *Chem. Rev.* **2004**, *104*, 4791.
- [2] R. A. De De Souza, J. A. Kilner, J. F. Walker, *Mater. Lett.* **2000**, *43*, 43.
- [3] A. Urushibara, Y. Moritomo, T. Arima, A. Asamitsu, G. Kido, Y. Tokura, *Phys. Rev. B* **1995**, *51*, 103.
- [4] Y. Tokura, Y. Tomioka, *J. Magn. Magn. Mater.* **1999**, *200*, 1.
- [5] A. Asamitsu, Y. Tomioka, H. Kuwahara, Y. Tokura, *Nature* **1997**, *388*, 50.
- [6] S. Q. Liu, N. J. Wu, A. Ignatiev, *Appl. Phys. Lett.* **2000**, *76*, 2749.
- [7] M.-H. Phan, S.-C. Yu, N. H. Hur, *Appl. Phys. Lett.* **2005**, *86*, 72504.
- [8] M. H. Phan, S. C. Yu, *J. Magn. Magn. Mater.* **2007**, *308*, 325.
- [9] C. Adamo, X. Ke, H. Q. Wang, H. L. Xin, T. Heeg, M. E. Hawley, W. Zander, J. Schubert, P. Schiffer, D. A. Muller, L. Maritato, D. G. Schlom, *Appl. Phys. Lett.* **2009**, *95*, 112504.
- [10] H. Boschker, M. Mathews, E. P. Houwman, H. Nishikawa, A. Vailionis, G. Koster, G. Rijnders, D. H. A. Blank, *Phys. Rev. B* **2009**, *79*, 1.
- [11] L. Yan, P. a Salvador, *ACS Appl. Mater. Interfaces* **2012**, *4*, 2541.
- [12] R. Gross, L. Alff, B. Büchner, B. H. Freitag, C. Höfener, J. Klein, Y. Lu, W. Mader, J. B. Philipp, M. S. R. Rao, P. Reutler, S. Ritter, S. Thienhaus, S. Uhlenbruck, B. Wiedenhorst, *J. Magn. Magn. Mater.* **2000**, *211*, 150.
- [13] A. M. Saranya, D. Pla, A. Morata, A. Cavallaro, J. Canales-Vázquez, J. A. Kilner, M. Burriel, A. Tarancón, *Adv. Energy Mater.* **2015**, *5*, 1500377.
- [14] E. Navickas, T. M. Huber, Y. Chen, W. Hetaba, G. Holzlechner, G. Rupp, M. Stöger-Pollach, G. Friedbacher, H. Hutter, B. Yildiz, J. Fleig, *Phys. Chem. Chem. Phys.* **2015**, *17*, 7659.

- [15] F. Chiabrera, A. Morata, M. Pacios, A. Tarancón, *Solid State Ionics* **2017**, 299, 70.
- [16] E. Navickas, Y. Chen, Q. Lu, W. Wallisch, T. M. Huber, J. Bernardi, M. Stöger-Pollach, G. Friedbacher, H. Hutter, B. Yildiz, J. Fleig, *ACS Nano* **2017**, 11, 11475.
- [17] A. Saranya, A. Morata, D. Pla, M. Burriel, F. Chiabrera, I. Garbayo, A. Hornés, J. Kilner, A. Tarancón, *Chem. Mater.* **2018**, *accepted*, acs. chemmater.8b01771.
- [18] D. Marrocchelli, L. Sun, B. Yildiz, *J. Am. Chem. Soc.* **2015**, 137, 4735.
- [19] L. Sun, D. Marrocchelli, B. Yildiz, *Nat. Commun.* **2015**, 6, 6294.
- [20] S. Kar, J. Sarkar, B. Ghosh, a. Raychaudhuri, *Phys. Rev. B* **2006**, 74, 85412.
- [21] A. Gupta, G. Q. Gong, G. Xiao, P. R. Duncombe, P. Lecoeur, P. Trouilloud, Y. Y. Wang, V. P. Dravid, J. Z. Sun, *Phys. Rev. B* **1996**, 54, R15629.
- [22] I. Fina, G. Apachitei, D. Preziosi, H. Deniz, D. Kriegner, X. Marti, M. Alexe, *Sci. Rep.* **2015**, 5, 1.
- [23] J. To, J. B. Goodenough, *J. Solid State Chem.* **1997**, 128, 117.
- [24] I. Marozau, P. T. Das, M. Döbeli, J. G. Storey, M. a. Uribe-Laverde, S. Das, C. Wang, M. Rössle, C. Bernhard, *Phys. Rev. B* **2014**, 89, 174422.
- [25] J. Chen, M. Döbeli, D. Stender, K. Conder, A. Wokaun, C. W. Schneider, T. Lippert, *Appl. Phys. Lett.* **2014**, 105, 114104.
- [26] S. Wicklein, A. Sambri, S. Amoruso, X. Wang, R. Bruzzese, A. Koehl, R. Dittmann, *Appl. Phys. Lett.* **2012**, 101, DOI 10.1063/1.4754112.
- [27] S. Y. Choi, S. D. Kim, M. Choi, H. S. Lee, J. Ryu, N. Shibata, T. Mizoguchi, E. Tochigi, T. Yamamoto, S. J. L. Kang, Y. Ikuhara, *Nano Lett.* **2015**, 15, 4129.
- [28] M. Varela, M. P. Oxley, W. Luo, J. Tao, M. Watanabe, A. R. Lupini, S. T. Pantelides, S. J. Pennycook, *Phys. Rev. B - Condens. Matter Mater. Phys.* **2009**, 79, 1.
- [29] S. P. Waldow, R. A. De Souza, *ACS Appl. Mater. Interfaces* **2016**, 8, 12246.
- [30] T. Mayeshiba, D. Morgan, *Solid State Ionics J.* **2017**, 17, 2715.
- [31] J. M. Polfus, B. Yildiz, H. L. Tuller, *Phys. Chem. Chem. Phys.* **2018**, 20, 19142.
- [32] D. J. Keeble, S. Wicklein, L. Jin, C. L. Jia, W. Egger, R. Dittmann, *Phys. Rev. B* **2013**, 87, 195409.
- [33] M. D. Scafetta, S. J. May, *Phys. Chem. Chem. Phys.* **2017**, 19, 10371.
- [34] F. Chiabrera, I. Garbayo, D. Pla, M. Burriel, F. Wilhelm, A. Rogalev, M. Núñez, A. Morata, A. Tarancón, *APL Mater.* <https://doi.org/10.1063/1.5054576>.
- [35] J. Vergara, V. Madurga, *Phys. Rev. B* **1999**, 60, 1127.
- [36] S. Hébert, B. Wang, A. Maignan, C. Martin, R. Retoux, B. Raveau, *Solid State Commun.* **2002**, 123, 311.
- [37] C. Zener, *Phys. Rev.* **1951**, 82, 403.

- [38] A. J. Millis, P. B. Littlewood, B. I. Shraiman, *Phys. Rev. Lett.* **1995**, *74*, 5144.
- [39] Y. Choi, M. C. Lin, M. Liu, *J. Power Sources* **2010**, *195*, 1441.
- [40] Y. A. Mastrikov, R. Merkle, E. Heifets, E. A. Kotomin, J. Maier, *J. Phys. Chem. C* **2010**, *114*, 3017.
- [41] R. A. De Souza, *J. Mater. Chem. A* **2017**, *5*, 20334.
- [42] L. Wang, R. Merkle, Y. a. Mastrikov, E. a. Kotomin, J. Maier, *J. Mater. Res.* **2012**, *27*, 2000.
- [43] W. Jung, H. L. Tuller, *Adv. Energy Mater.* **2011**, *1*, 1184.
- [44] M. Wolcyrz, R. Horyn, F. Bouree, E. Bukowska, *J. Alloys Compd.* **2003**, *353*, 170.
- [45] D. H. Ji, S. L. Wang, X. Z. Ge, Q. Q. Zhang, C. M. Zhang, Z. W. Zeng, Y. Bai, *Phys. Chem. Chem. Phys.* **2017**, *19*, 17121.
- [46] N. Bagués, J. Santiso, B. D. Esser, R. E. A. Williams, D. W. McComb, Z. Konstantinovic, L. Balcells, F. Sandiumenge, *Adv. Funct. Mater.* **2018**, 1704437.
- [47] K. Song, K. Du, H. Ye, *Micron* **2017**, *96*, 72.
- [48] Y. Feng, K. Jin, L. Gu, X. He, C. Ge, Q. Zhang, M. He, Q. Guo, Q. Wan, M. He, H. Lu, G. Yang, *Sci. Rep.* **2016**, *6*, 22382.
- [49] Z. Li, M. Bosman, Z. Yang, P. Ren, L. Wang, L. Cao, X. Yu, C. Ke, M. B. H. Breese, A. Rusydi, W. Zhu, Z. Dong, Y. L. Foo, *Adv. Funct. Mater.* **2012**, *22*, 4312.
- [50] S. Estradé, J. M. Rebled, J. Arbiol, F. Peiró, I. C. Infante, G. Herranz, F. Sánchez, J. Fontcuberta, R. Córdoba, B. G. Mendis, A. L. Bleloch, *Appl. Phys. Lett.* **2009**, *95*, 1.
- [51] J. Nowotny, M. Rekas, *J. Am. Ceram. Soc.* **1998**, *81*, 67.
- [52] M. D. Segall, P. J. D. Lindan, M. J. Probert, C. J. Pickard, P. J. Hasnip, S. J. Clark, M. C. Payne, *J. Phys. Condens. Matter* **2002**, *14*, 2717.
- [53] C. Payne, N. York, *Rev. Mod. Phys.* **1992**, *64*, 1045.
- [54] J. P. Perdew, K. Burke, M. Ernzerhof, *Phys. Rev. Lett.* **1996**, *77*, 3865.
- [55] D. Vanderbilt, *Phys. Rev. B* **1990**, *41*, 7892.
- [56] H. J. Monkhorst, J. D. Pack, *Phys. Rev. B* **1978**, *13*, 5897.
- [57] R. J. Nicholls, A. J. Morris, C. J. Pickard, J. R. Yates, *J. Phys. Conf. Ser.* **2012**, *371*, 12062.
- [58] A. J. Morris, R. J. Nicholls, C. J. Pickard, J. R. Yates, *Comput. Phys. Commun.* **2014**, *185*, 1477.

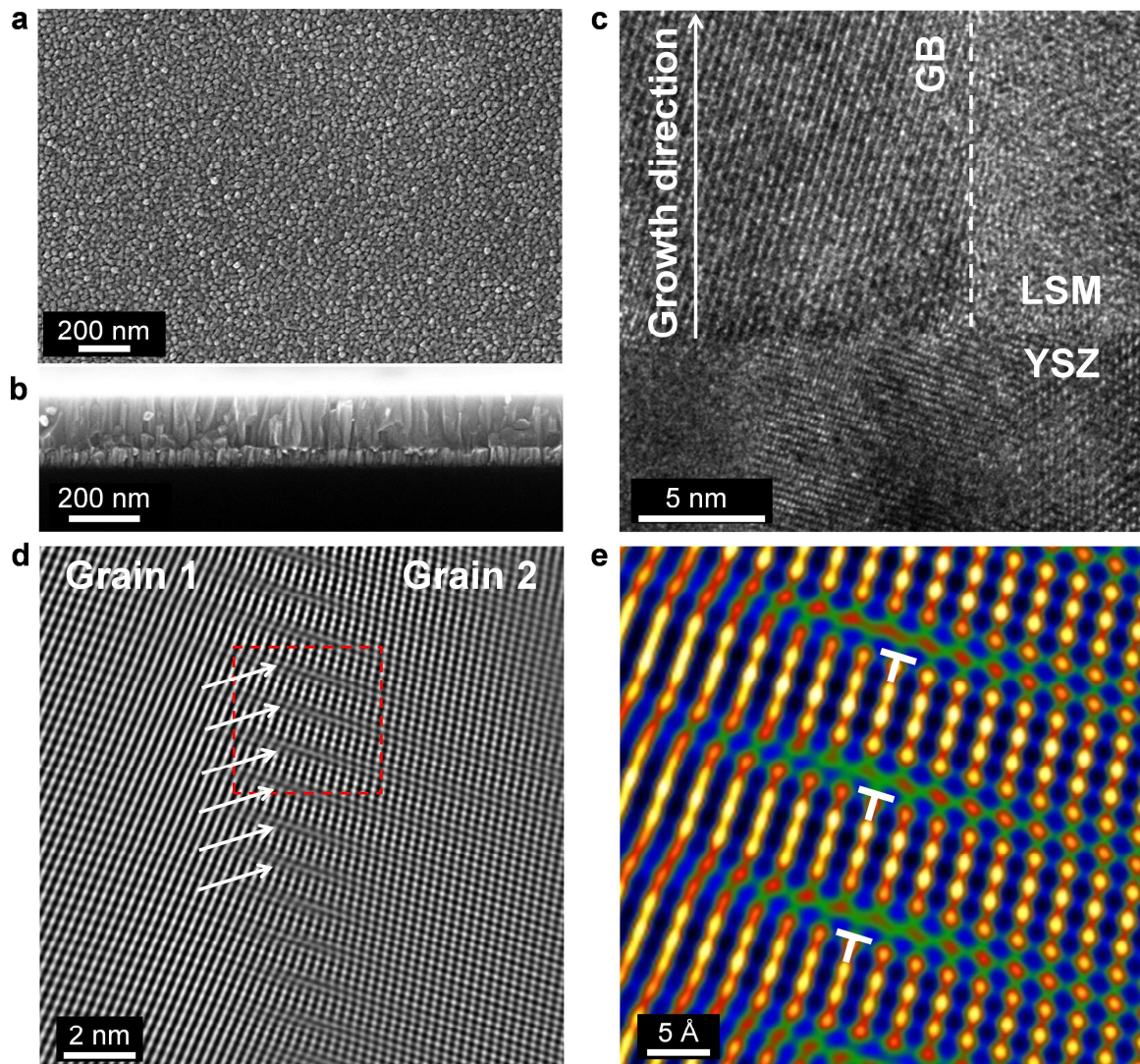


**Figure 1.** **a**, SEM top-view and **b**, cross-section of the fully-dense and columnar LSM/YSZ bi-layer grown on the top of  $\text{Si}_3\text{N}_4/\text{SiO}_2/\text{Si}$ . **c**, HRTEM image of YSZ/LSM interface showing one grain boundary (highlighted by a white dashed line) oriented in a direction perpendicular respect to the substrate. **d**, Fourier filtered image of a LSM grain boundary consisting of a dense pattern of dislocations repeating every  $\sim 1$  nm. **e**, coloured enlargement of the red dotted square shown in **d**, in which 3 dislocations are highlighted by white “T” symbols.

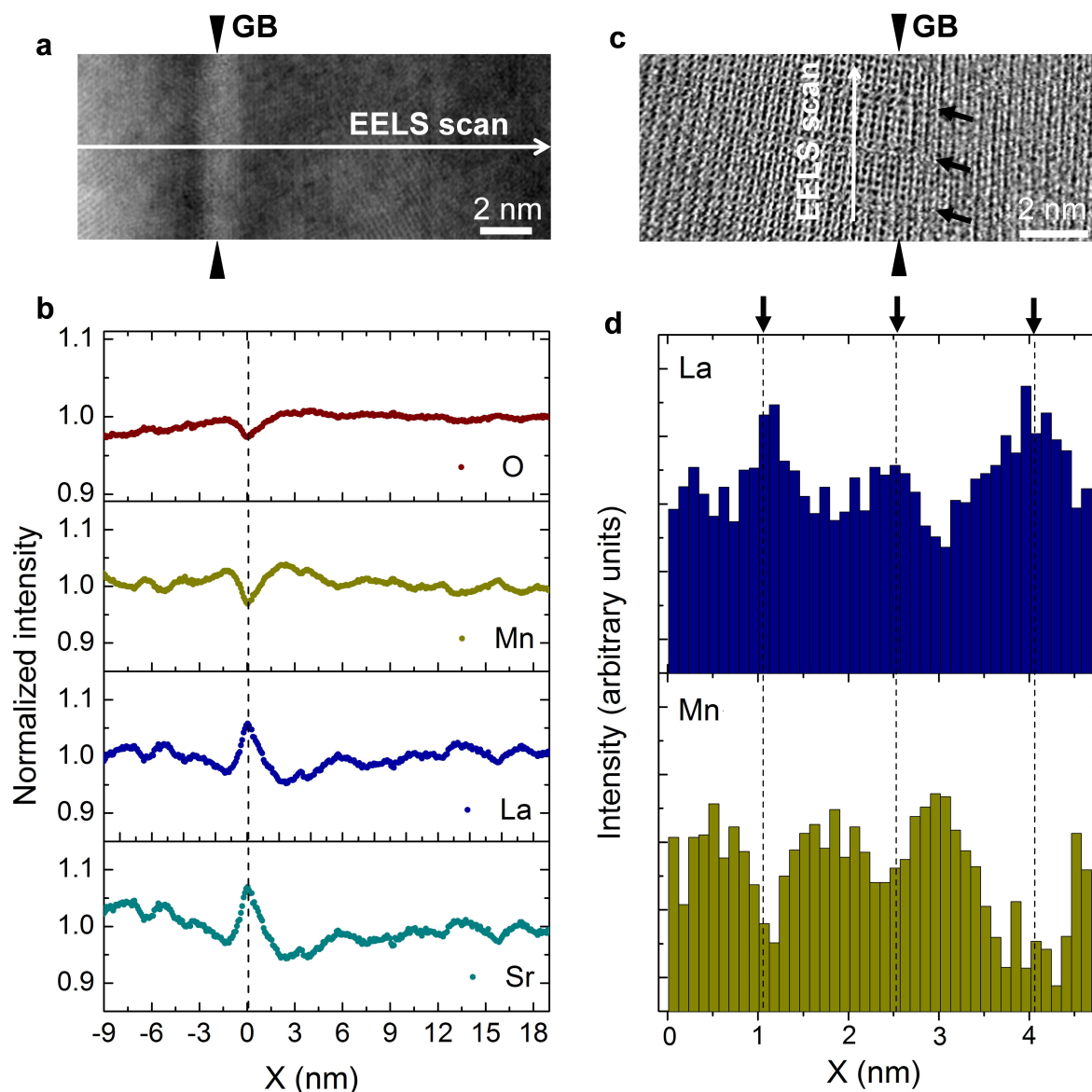


**Figure 2.** **a**, HAADF image of the GB, showing a different contrast at the interface. **b**, chemical composition obtained from the EELS scan across the GB (white arrow in **a**). Integrated intensity signals were normalized to the grain (bulk) values for each element. A significant compositional variation is visible near the GB interface. **c**, Bright field HRTEM figure of a grain boundary showing atomic fringes at the interface (indicated by black arrows) that agree with the dislocations pattern observed in **Figure 1.c**. **d**, La and Mn variation extracted from EELS scan along the GB (white arrow in **c**). A simultaneous increase of La and decrease of Mn concentration is observed at specific locations that correspond well with the fringe pattern observed, indicating that the chemical variations occurs in the proximity of the dislocations.

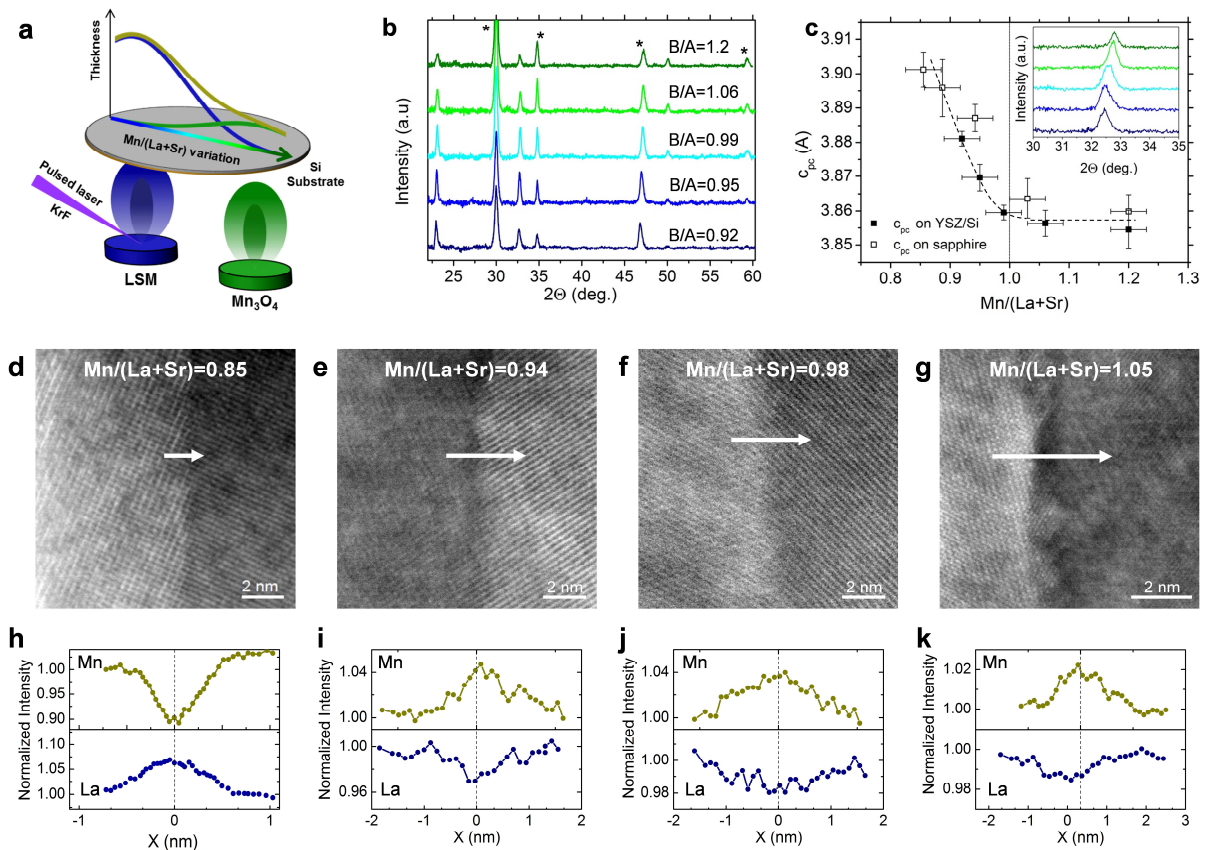


**Figure 3.** **a.** Sketch of the combinatorial approach used for varying B/A ratio. **b.** XRD of  $\text{LSM}_y$  samples deposited on YSZ/Si for different B/A ratio. Black asterisk marks the YSZ diffraction peaks. **c.** Evolution of pseudo-cubic lattice parameter obtained by XRD for different Mn content. The inset shows the shift of the 110 peak in the samples deposited on sapphire (0001). **d-g,** Annular dark field images of grain boundaries in samples with different B/A ratio and **h-k** corresponding La and Mn variation extracted from EELS scans. A sudden decrease of La and a progressive increase of Mn are obtained in the GBs changing the overall B/A ratio in the thin films.

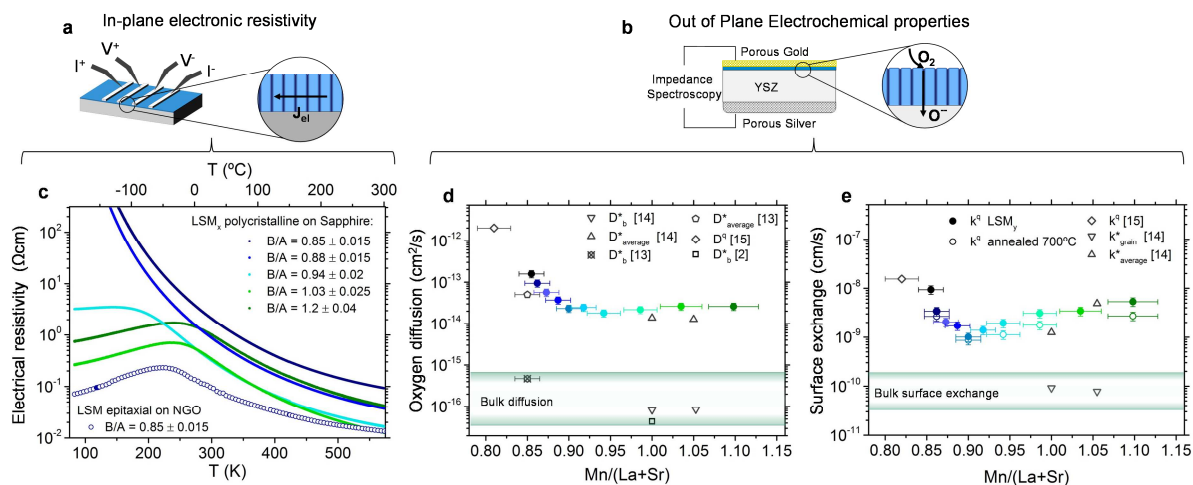


**Figure 4.** **a.** Sketch of the in-plane electrical measurement and **c.** resistivity obtained as a function of temperature for different B/A ratio. Results obtained for the epitaxial  $\text{LSM}_{0.85}$  are reported for comparison **b.** Scheme of the electrochemical measurements. The columnar structures of the films offer a preferential ionic pathway along the grain boundaries. Oxygen diffusion (**d**) and surface exchange coefficient (**e**), extracted from the impedance at  $650^{\circ}\text{C}$  in air for different B/A ratio. Diffusion coefficients measured in SIMS experiments by Saranya et al.,<sup>[13]</sup> Navickas et al.,<sup>[14]</sup> De Souza et al.<sup>[2]</sup> and in EIS by Chiabrera et al.<sup>[15]</sup> are reported for comparison. Stoichiometry of films from references<sup>[13,15]</sup> were measured within the frame of this work.

**Table 1.** Formation energy of  $La_{Mn}^{\times}$  defect calculated by DFT in different configurations.

Formation energy (eV)		Without $V_{\text{O}}^{\bullet}$			With one $V_{\text{O}}^{\bullet}$		
		$\epsilon = 0$	$\epsilon = 1\%$	$\epsilon = 2\%$	$\epsilon = 0$	$\epsilon = 1\%$	$\epsilon = 2\%$
# $Sr'_{La}$	<b>0</b>	5.25	-	-	2.29	-	-
	<b>1</b>	3.36	3.34	3.43	2.61	2.58	2.66
	<b>3</b>	2.96	2.48	2.13	2.32	2.35	2.3